the dominant force associated with the motion of such screw dislocations (*19*). At the onset of dislocation growth, we estimated the magnitude of each of the forces to be on the order of 100 fN. The length of a dislocation as a function of time can be calculated from the force balance, $F_{PK} = F_l + F_d$ (*23*). As the dislocation grows and accommodates an increasing portion of the misfit strain, the elastic force driving the expansion decreases. Thus, the force balance predicts that $L = L_{inf}[1 - \exp(-t/\tau)]$, where L_{inf} is the final dislocation length and τ is a constant, proportional to the ratio of the viscosity of the solvent to the elastic modulus.

To test this prediction, we scaled the entire data set and plotted L/L_{inf} versus t/τ (Fig. 4C). The data are in excellent agreement with the theoretical prediction. As a final check, we used the average value of τ, which we determined to be 130 (±40) s, to estimate the elastic modulus of the colloidal crystal (*23*). This estimate yields a value of 0.3 Pa, in reasonable agreement with theoretical estimates that predict a value on the order of 1 Pa (*7*). This is one of the only techniques available for directly determining the elastic modulus of thin colloidal crystal films.

The combination of imaging techniques presented and the close similarity of dislocations in colloidal and atomic crystals lays the groundwork for investigating further important phenomena that cannot be directly studied on the atomic scale, such as the nucleation and interaction of dislocations in very constrained systems. The remarkable and unexpected correspondence between continuum model predictions and the phenomena we observe on the scale of just a few lattice constants suggests that continuum models may also be applied to describe dislocation behavior even in highly constrained structures, such as those being made as nanoscale science pushes to ever smaller devices. Finally, the effects of the vanishing stacking fault energy and the pressure head on dislocations in colloidal crystals highlight some of the unique features of this class of condensed matter.

References and Notes

1. J. P. Hirth, J. Lothe, *Theory of Dislocations* (Wiley, New York, ed. 2, 1982).
2. G. I. Taylor, *Proc. R. Soc. A* **145**, 362 (1934).
3. E. Orowan, *Z. Phys.* **89**, 605 (1934).
4. M. Polanyi, *Z. Phys.* **89**, 660 (1934).
5. J. Lepinoux, D. Maziere, V. Pontikis, G. Saada, Eds., *NATO Science Series E, Multiscale Phenomena in Plasticity: From Experiments to Phenomenology, Modeling and Materials Engineering* (Kluwer Academic, Dordrecht, Netherlands, 2000), vol. 367.
6. A. D. Dinsmore, E. R. Weeks, V. Prasad, A. C. Levitt, D. A. Weitz, *Appl. Opt.* **40**, 4152 (2001).
7. D. Frenkel, A. J. C. Ladd, *Phys. Rev. Lett.* **59**, 1169 (1987).
8. R. Hull, J. C. Bean, D. J. Werder, R. E. Leibenguth, *Appl. Phys. Lett.* **52**, 1605 (1988).
9. A. van Blaaderen, R. Ruel, P. Wiltzius, *Nature* **385**, 321 (1997).
10. The silica particles (Micromod, Sicastar, 1.5 μm) are suspended in an index-matching mixture of water and dimethyl sulfoxide at an initial volume fraction of 0.03%. We add a small amount of a fluorescein-NaOH mixture to the solvent, allowing us to image the particles with fluorescence under the confocal microscope; the particles appear as dark spheres in a light background.
11. We use standard photolithographic processes to prepare a template with a square array of 3000 by 3000 holes in a polymethyl methacrylate layer 500 nm thick over an area of about 5 mm by 5 mm.
12. For example, we estimate that increasing the film thickness from 20 μm to 30 μm produces a 0.4% decrease in the preferred lattice spacing.
13. D. B. Williams, C. B. Carter, *Transmission Electron Microscopy: A Textbook for Materials Science* (Plenum, New York, 1996).
14. D. Hull, D. J. Bacon, *Introduction to Dislocations* (Pergamon, New York, 1984).
15. S. Pronk, D. Frenkel, *J. Chem. Phys.* **110**, 4589 (1999).
16. F. C. Frank, J. H. van der Merwe, *Proc. R. Soc. London Ser. A* **198**, 216 (1949).
17. J. W. Matthews, A. E. Blakeslee, *J. Cryst. Growth* **27**, 118 (1974).
18. In accordance with the one-dimensional dislocation model, we assume that the x and y directions are uncoupled and study the accommodation of the misfit strain in one spatial direction. The elastic energy stored in a strained film of thickness h is $U_{el} = \frac{1}{2}\varepsilon_{el}^2 Eh$ per unit area, where the elastic strain is $\varepsilon_{el} = \varepsilon_0 - \varepsilon$, and ε is the strain relieved by the dislocations. The energy cost per unit area associated with the misfit dislocations is $U_l = (\Lambda^{-1})\{\mu b^2 \ln(R/r_c)/[4\pi(1-\nu)]\}$, where b is the magnitude of the Burgers vector of the dislocations, and r_c and R are the core and outer radii of the dislocation strain field, respectively (*1*). Minimizing the total energy $U_{el} + U_l$ with respect to the number of dislocations per unit length Λ^{-1}, we find that, for film thicknesses greater than h_c, the equilibrium dislocation density is $\Lambda^{-1} = [\varepsilon_0/(b \cos\alpha)] - \{\mu \ln(R/r_c)/[4\pi(1-\nu)E \cos^2\alpha\, h]\}$. As the film thickness increases, the dislocation density approaches the limit $[\varepsilon_0/(b \cos\alpha)]$, where the entire misfit strain is accommodated by dislocations. The critical film thickness, where $\Lambda^{-1} = 0$, is $h_c = \mu b \ln(R/r_c)/[4\pi E\varepsilon_0(1-\nu)\cos\alpha]$; this yields a critical thickness $h_c = 22$ μm.
19. M. Jorand, F. Rothen, P. Pieranski, *J. Phys. (Paris)* **46**, 245 (1985).
20. We note that this value for the strain ε is larger than that predicted for this 31-μm-thick film grown on a template where $\varepsilon_0 = 0.015$. However, the model prediction depends sensitively on the value of the misfit strain ε_0. For example, a 0.005 increase in the misfit strain can account for the discrepancy. Such an increase can result from the change in pressure head when the film thickness changes from 20 μm to 30 μm.
21. The elastic energy stored in the thin crystal layer below the dislocations is $U_{el} = \frac{1}{2}\varepsilon_0^2 Ez$ per area and decreases with decreasing distance, z, of the dislocations to the template. Hence, a single dislocation experiences the elastic force $F_{el} = \frac{1}{2}\Lambda E\varepsilon_0^2$.
22. J. W. Matthews, S. Mader, T. B. Light, *J. Appl. Phys.* **41**, 3800 (1970).
23. The forces acting on the screw dislocation are given by $F_{PK} = 2\mu(1+\nu)hb \cos\alpha\, \varepsilon_{el}/(1-\nu)$, $F_l = \mu b^2 \ln(R/r_c)/[4\pi(1-\nu)]$, and $F_d = (h/\sin\alpha)\gamma v$, where $\gamma = \eta b^2/4\pi r_c^2$, v is the velocity of the screw dislocations, and η is the solvent viscosity. As the dislocation expands, it accommodates an increasing portion of the misfit strain. The rate at which the strain is accommodated is $d\varepsilon/dt = \rho_{screw}\, b \cos\alpha\, v$, where ρ_{screw} is the number of mobile screw dislocations per unit area of the film. From the force balance $F_{PK} = F_l + F_d$, we find that $\varepsilon(t) = \varepsilon_{inf}[1 - \exp(-t/\tau)]$, where the constant $\varepsilon_{inf} = \varepsilon_0 - \{b \ln(R/r_c)/[8\pi(1+\nu)h \cos\alpha]\}$ corresponds to the final misfit strain accommodated by the dislocation, and the time constant $\tau = (1-\nu)\gamma/(Eb^2 \cos^2\alpha \sin\alpha\, \rho_{screw})$. Because ε is proportional to the dislocation length L, this equation predicts the time dependence of L. To calculate the elastic modulus from the measured time constant τ, we determine the density of mobile screw dislocations by counting the number of dislocations that are expanding, multiplying by 2, and dividing by the area corresponding to the field of view. We obtain $\rho_{screw} = 3 \times 10^{-4}$ μm^{-2}. Taking $\eta = 3.0 \times 10^{-3}$ Pa·s (*24*), we obtain a value of 0.3 Pa for the elastic modulus.
24. Y. Higashigaki, D. H. Christensen, C. H. Wang, *J. Phys. Chem.* **85**, 2531 (1981).

25. We thank R. Christianson and D. Blair for their help with the image analysis, and E. Chen and Y. Lu for their help in manufacturing the templates. Supported by a Lynen Fellowship from the Alexander von Humboldt Foundation (P.S.), by NSF grant DMR-0243715, and by Harvard MRSEC grant DMR-0213805.

Supporting Online Material

www.sciencemag.org/cgi/content/full/305/5692/1944/DC1

Movie S1

30 June 2004; accepted 20 August 2004

Ice Flow Direction Change in Interior West Antarctica

Martin J. Siegert,[1]* Brian Welch,[2] David Morse,[3] Andreas Vieli,[1] Donald D. Blankenship,[3] Ian Joughin,[4] Edward C. King,[5] Gwendolyn J.-M. C. Leysinger Vieli,[1] Antony J. Payne,[1] Robert Jacobel[2]

Upstream of Byrd Station (West Antarctica), ice-penetrating radar data reveal a distinctive fold structure within the ice, in which isochronous layers are unusually deep. The fold has an axis more than 50 kilometers long, which is aligned up to 45° to the ice flow direction. Although explanations for the fold's formation under the present flow are problematic, it can be explained if flow was parallel to the fold axis ~1500 years ago. This flow change may be associated with ice stream alterations nearer the margin. If this is true, central West Antarctica may respond to future alterations more than previously thought.

Ice-penetrating radar provides information on ice thickness, subglacial morphology, and internal layering, caused by electromagnetic-wave reflections from dielectric contrasts (such as high-acidity horizons formed from the aerosol product of volcanic events contained within ancient snow). Internal layers are believed to be isochronous, as

they obey the rules of stratigraphy (*1*). They are often traceable continuously over several hundred kilometers. In slow-flowing regions of ice sheets, internal layers commonly drape over topography (i.e., their vertical position relates to bed relief). In ice streams and their tributaries, however, internal layers may deform in a manner unrelated to bed topography (*2*, *3*). In one location upstream of the tributaries of Ice Stream D in West Antarctica (Fig. 1), the internal layer pattern differs markedly from the bed topography. Along the present ice flow line, internal layers drop in elevation by up to 800 m (over horizontal distances of ~5 km) without substantial variation in bed morphology (Fig. 2A), and then return to their approximate original elevation downstream. This highly unusual internal layer fold is observed in several radar transects, and the axis of the fold is aligned roughly linearly (XY in Fig. 1). At Y, the alignment is at ~45° to the current flow direction, whereas ice flows roughly parallel to the axis at X (Fig. 1). Internal layers are easily traceable in the radar data, allowing the internal layer depths to be determined along XY. This longitudinal section shows the steady internal layer convergence to the bed from X to Y, in contrast to the short-wavelength, high-amplitude fold in the cross direction AA′ and BB′ (Fig. 2), which also demonstrates how the fold amplitude increases from X to Y (fig. S1).

Under the present glaciological setting, six processes that may distort internal layers within a grounded ice sheet can be ruled out as explanations for the fold. First, basal topography is relatively subdued upstream of the layer distortion and so, under the present glaciological regime, there is little ice flow around subglacial obstacles. Second, strain rate variations in the ice can cause internal layer distortions known as Raymond bumps (*4*). These occur at the ice sheet divide, require a frozen bed (*5*), and increase in size with depth quadratically. Raymond bumps differ from the measured layers, which are located ~180 km from the ice divide and increase in size linearly with ice depth (fig. S1). Moreover, as we discuss later, the radar data show evidence of warm subglacial conditions. Third, changes to the surface accumulation rate can cause internal layer distortions where there is an alteration to the ice sheet surface slope (*6*). There is, however, no noticeable surface-slope variation around the measured layers (*7*), and furthermore, the slope of the fold's axial plane (dipping upstream, Fig. 3A and fig. S1) is the opposite of what would be expected from a nonuniform but stationary pattern of surface accumulation. Fourth, interferometric synthetic aperture radar (InSAR) data (*8*, *9*) reveal little ice sheet convergence or divergence over the fold, thus ruling out converging or diverging ice flow as an explanation. Fifth, isochrones may dip toward the ice base across the transition between regions of no-sliding and sliding and toward the ice surface across a transition from sliding to no-sliding (*10*). Although the structure at BB′ could be accounted for under this mechanism, the fold's amplitude is so great at AA′ that it could not have formed without substantial acceleration (and then deceleration) to the ice flow. InSAR data show no such velocity anomaly around AA′, so it appears unlikely that ice flow over no-sliding/sliding/no-sliding zones could have formed the fold at this location. Sixth, the convergence of internal layers with the ice base can be assigned to enhanced geothermal heating and the resulting basal melting of ice (*11*). We calculate that the convergence of the

[1]Centre for Polar Observation and Modelling, Bristol Glaciology Centre, School of Geographical Sciences, University of Bristol, Bristol BS8 1SS, UK. [2]Physics Department, St. Olaf College, Northfield, MN 55057, USA. [3]Institute for Geophysics, John A. and Katherine G. Jackson School of Geosciences, The University of Texas, 4412 Spicewood Springs Road, Austin, TX 78759, USA. [4]Jet Propulsion Laboratory, Mail Stop 300-235, 4800 Oak Grove Drive, Pasadena, CA 91109, USA. [5]Physical Sciences Division, British Antarctic Survey, High Cross, Madingley Road, Cambridge CB3 0ET, UK.

*To whom correspondence should be addressed. E-mail: m.j.siegert@bristol.ac.uk

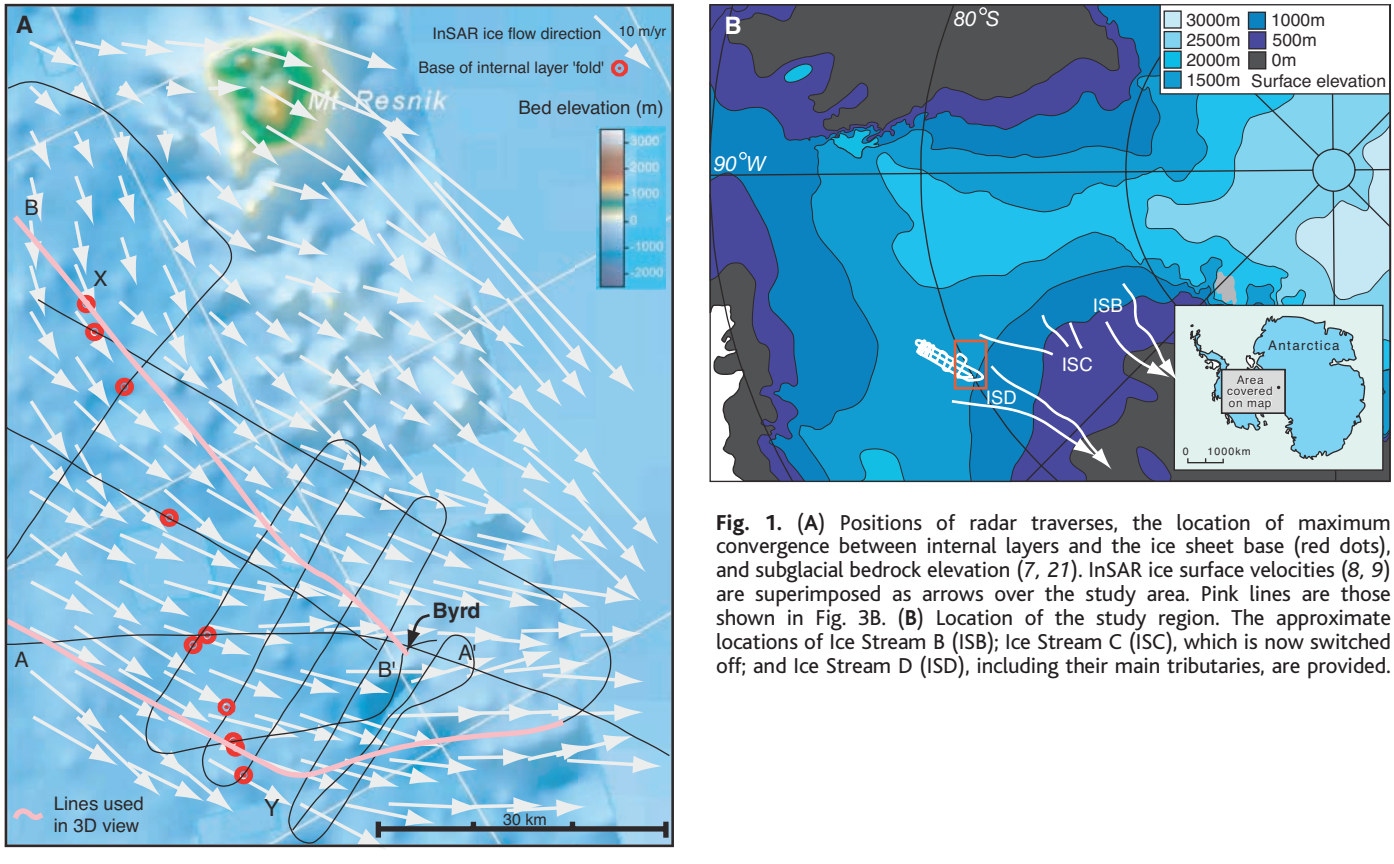

Fig. 1. (**A**) Positions of radar traverses, the location of maximum convergence between internal layers and the ice sheet base (red dots), and subglacial bedrock elevation (*7*, *21*). InSAR ice surface velocities (*8*, *9*) are superimposed as arrows over the study area. Pink lines are those shown in Fig. 3B. (**B**) Location of the study region. The approximate locations of Ice Stream B (ISB); Ice Stream C (ISC), which is now switched off; and Ice Stream D (ISD), including their main tributaries, are provided.

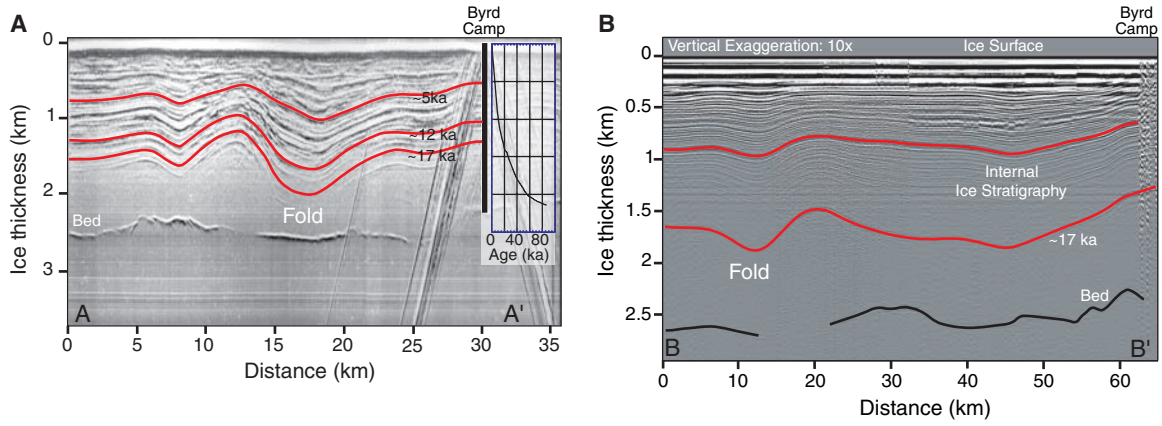

Fig. 2. (**A**) Radar data upstream of the Byrd ice core along AA′ (located in Fig. 1). These radar data were collected by members of the Scott Polar Research Institute (Cambridge, UK) in 1974 to 1975, using a frequency of 60 MHz and a pulse width of 250 ns. Radar reflections off the various buildings of Byrd Station are seen as surface hyperbolas. Layers have been dated at their intersection with the ice core site at Byrd Station (*22*). ka, thousand years ago. (**B**) Radar data along BB′ (located in Fig. 1). These data were collected by the US-ITASE program in 2001, using a frequency of 3 MHz (*23*). The deepest layer (highlighted in red) is an unusually bright internal layer between ice depths of 1250 and 1750 m, which has an age of 17,000 years (*22*). The intersection of the radar transect with XY is where the internal layer fold is at its deepest (i.e., the trough minima).

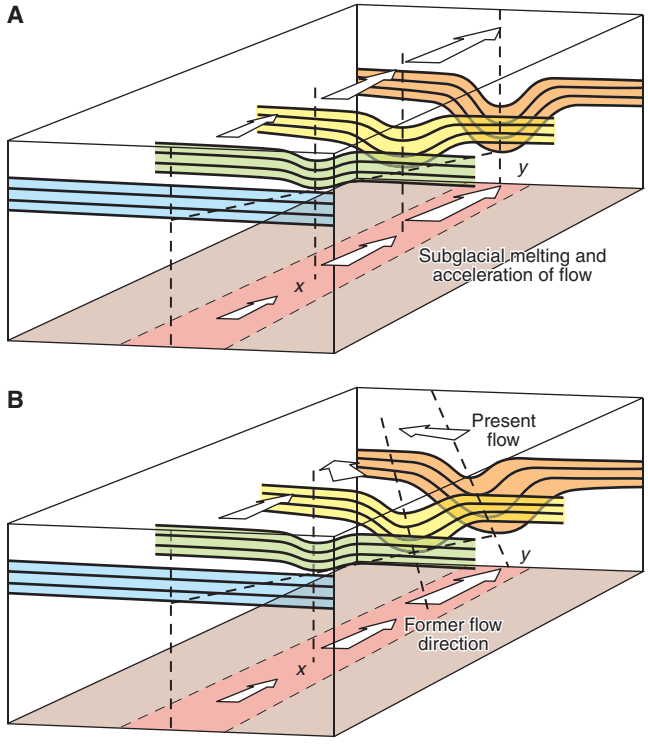

Fig. 3. Conceptual development of the englacial fold. (**A**) The fold forms as a consequence of ice flow across a no-sliding/sliding zone and subglacial melting. The fold axis forms parallel to ice flow and the amplitude of the fold increases from X to Y. (**B**) Ice flow change results in flow across the fold axis, which causes secondary deformation to the fold. At Y, the deformation is greatest (the axis here is aligned 45° to ice flow), which results in the tilting of the axial plane (dipping upstream). The fold axis remains roughly linear, which is consistent with the fact that fast ice flow (basal sliding) no longer occurs here.

internal layers with the ice base would require melt rates of up to 6 cm year^{-1}. Such melt rates are an order of magnitude greater than those calculated for the Siple Coast region through consideration of ice flow and heat transfer (*12*). Although we can use basal melting to explain how isochrones can be drawn down to greater depths, it cannot explain how the layers appear at much higher elevations immediately downstream.

The presence of subglacial water (the product of basal melting) is supported, however, by the relative strengths of bed echoes. Internal layer convergence with the bed is associated with bed returns as strong as one would expect from an ice-water interface (Fig. 2A). In point of fact, near the ice divide, radar data reveal a small subglacial lake (*13*), the surface of which has an echo strength similar to that beneath the internal layer fold. Subglacial melting cannot, therefore, be ruled out as a process contributing to the shape of the internal layers.

As there is no apparent explanation for the fold under the current glaciological setting, explanations involving an alternative (former) glaciological setting are examined. The rationale for this is as follows. First, the current ice sheet configuration in West Antarctica is thought to have been achieved ~6000 years ago, after a prolonged period during which the grounded margin was positioned near the present ice shelf terminus (*14*–*16*). Hence, the flow pattern around Byrd Station may have been different 6000 years ago. Second, investigations of Ice Stream C have shown that internal layer structures (similar to those in Fig. 2) within regions of enhanced ice flow can be traced along the line of ice flow (*3*). Because of ice sheet convergence, the layer structures compress laterally down the flowline. As the fold upstream of Byrd Station appears similar to the structures observed in Ice Stream C (i.e., a traceable englacial structure with extended fold axes and no apparent link to bed perturbation), we propose that the fold axis is a paleoflow line (Fig. 1) (translated only partially by subsequent sliding, as discussed later). This rationale reopens the possibility of two explanations discounted previously: (i) ice flow around subglacial topography, and (ii) processes acting on the ice as it flows from X to Y (Fig. 1).

The most obvious subglacial feature that may be responsible for the internal layer distortion is Mount Resnik, a huge subglacial mountain located 30 km from X (Fig. 1). However, the fold axis, XY, points to ice flow originating well upstream of Mount Resnik, making the mountain an unlikely source for the fold. Elsewhere, subglacial topography is subdued. The only remaining explanations involve englacial processes acting on the ice as it flows along the fold axis.

We propose that, when the flow was parallel to the axis, the fold may have been developed by a combination of basal melting and, because the fold increases in intensity from X to Y (fig. S1), sideways compression in a manner similar to that demonstrated for internal layers in Ice Stream C (*3*). We propose further that the formation of the fold was at, or upstream of, the fold in BB′ and due to flow across a no-sliding/sliding transition (*10*) (fig. S2). For this explanation to be correct, enhanced (ice stream tributary) flow must have occurred between X and Y. Such flow may require a wet ice base (to

allow basal sliding), which is consistent with the observation that there may be subglacial water directly beneath the fold axis.

Regardless of the actual mechanism responsible for the fold, it most probably formed before the establishment of the modern ice flow regime (*15*, *16*). At position X (Fig. 1), the inferred ice flow path (the fold axis) is close to the present-day ice flow vector and the fold is aligned vertically (Fig. 2B). Conversely, the fold axis across AA′ is aligned ~40° to the present flow vector, and the fold's axial plane is at a substantial angle to the vertical (increasing downstream to a maximum of 45°, dipping away from the direction of present ice flow) (Fig. 3 and fig. S1). We propose that when ice flowed parallel to the fold axis, the axial plane would have been vertical (as it is at X). Subsequently, under the present flow regime, the fold may be reworked by ice deformation acting to tilt the axial plane and basal sliding, which may "translate" the axis laterally. As the fold axis is straight, we contend that subglacial sliding is presently a minor component of ice flow. Ice deformation at 3 m $year^{-1}$, acting for 1000 years, would be sufficient to tilt the axial plane at X by ~45° (fig. S1). Timing of this order makes it possible that the change from paleo- to modern flow regimes is associated with measured alterations to ice streams C and D that occurred ~1500 years ago (*17*).

Currently, ice flows across much of the fold axis toward the southern tributary of Ice Stream D. Under the former ice flow regime, the direction of ice flow would have been toward the northern tributary of the same ice stream. Although evidence for ice flow change at the ice sheet margin has been observed on several occasions (*18*, *19*), this represents evidence of a major shift in the flow direction at the center of an ice sheet. The driver of this change could be associated with activation of the southern tributary of Ice Stream D a few thousand years ago. This activation may be related to the relaxation of the ice sheet from its pre-Holocene configuration that has been hypothesized from numerical modeling (*20*) or to changes to the internal ice sheet dynamics. In either case, the evidence for past flow change shows that interior regions of ice sheets may be affected by ice flow conditions downstream.

References and Notes

1. M. J. Siegert, R. C. A. Hindmarsh, G. S. Hamilton, *Quat. Res.* **59**, 114 (2003).
2. R. W. Jacobel, A. M. Gades, D. L. Gottschling, S. M. Hodge, D. L. Wright, *J. Glaciol.* **39**, 528 (1993).
3. F. Ng, H. Conway, *Geology* **32**, 481 (2004).
4. C. F. Raymond, *J. Glaciol.* **29**, 357 (1984).
5. E. C. Pettitt, P. H. Jacobson, E. D. Waddington, *Ann. Glaciol.* **37**, 370 (2003).
6. D. G. Vaughan, H. F. J. Corr, C. S. M. Doake, E. D. Waddington, *Nature* **298**, 323 (1999).
7. D. L. Morse, D. D. Blankenship, E. D. Waddington, T. A. Neumann, *Ann. Glaciol.* **35**, 36 (2002).
8. I. Joughin *et al.*, *Science* **286**, 283 (1999).
9. I. Joughin, S. Tulaczyk, R. Bindschadler, S. F. Price, *J. Geophys. Res.* **107**, 2289 (2002).
10. J. Weertman, *Quat. Res.* **6**, 203 (1976).
11. M. Fahnestock, W. Abdalati, I. Joughin, J. Brozena, P. Gogineni, *Science* **294**, 2338 (2001).
12. I. Joughin, S. Tulaczyk, D. R. MacAyeal, H. Engelhardt, *J. Glaciol.*, in press.
13. M. J. Siegert, J. A. Dowdeswell, M. R. Gorman, N. F. McIntyre, *Antarct. Sci.* **8**, 281 (1996).
14. H. Conway, B. L. Hall, G. H. Denton, A. M. Gades, E. D. Waddington, *Science* **286**, 280 (1999).
15. R. P. Ackert Jr. *et al.*, *Science* **286**, 276 (1999).
16. J. O. Stone *et al.*, *Science* **299**, 99 (2003).
17. R. W. Jacobel, T. A. Scambos, C. F. Raymond, A. M. Gades, *J. Geophys. Res.* **101**, 5499 (1996).
18. M. Fahnestock, T. Scambos, R. Bindschadler, G. Kvaran, *J. Glaciol.* **46**, 652 (2000).
19. R. W. Jacobel, T. A. Scambos, N. A. Nereson, C. F. Raymond, *J. Glaciol.* **46**, 102 (2000).
20. P. Huybrechts, *Quat. Sci. Rev.* **21**, 203 (2002).
21. M. B. Lythe, D. G. Vaughan, the BEDMAP Consortium, *J. Geophys. Res.* **106**, 11335 (2001).
22. T. Blunier, E. J. Brook, *Synchronization of the Byrd and Greenland (GISP2/GRIP) Records* [International Geosphere–Biosphere Programme Past Global Changes (IGBP PAGES)/World Data Center A for Paleoclimatology, Data Contribution Series #2001-003, 2001], available at www1.ncdc.noaa.gov/pub/data/paleo/icecore/antarctica/byrd/.
23. B. C. Welch, R. W. Jacobel, *Geophys. Res. Lett.* **30**, 1444 (2003).

24. We thank J. Dowdeswell, Director of the Scott Polar Research Institute, for access to radar records held there in archive. Supported by the Natural Environment Research Council (NERC) Centre for Polar Observation and Modelling, NERC grant no. NER/A/S/2001/01011, and a Philip Leverhulme Prize to M.J.S. U.S.–International Trans-Antarctic Scientific Expedition (US–ITASE) work was supported by National Science Foundation grant no. OPP-9814574.

Supporting Online Material

www.sciencemag.org/cgi/content/full/305/5692/1948/DC1
Materials and Methods
Figs. S1 and S2
Table S1
References and Notes

4 June 2004; accepted 23 August 2004

Fractionation of the Platinum-Group Elements During Mantle Melting

Conny Bockrath,* Chris Ballhaus, Astrid Holzheid

Experiments in sulfide-silicate systems demonstrate that two sulfide phases are stable in the asthenospheric upper mantle: a crystalline osmium-iridium-ruthenium–enriched monosulfide and a rhodium-platinum-palladium–enriched sulfide melt. During silicate melt segregation, monosulfide stays in the solid residue, dominating the noble metal spectrum of residual mantle. The sulfide melt is entrained as immiscible droplets in the segregating silicate melt, defining the noble metal inventory of the basaltic component.

When primitive mantle, chondritic with respect to the platinum-group elements (PGEs) (*1*), undergoes partial melting, the noble metals become fractionated. Os, Ir, and Ru are retained in the mantle residue, whereas Re, Pt, and Pd are sequestered to the basaltic melt (*2*). There is consensus that sulfide plays a major role in the fractionation process (*3*, *4*) because the PGEs of the mantle reside to a large extent in sulfide (*5*). But how fractionation is possible in the presence of sulfide, or whether sulfide must be eliminated to release any PGEs to the silicate melt (*6*), are unresolved issues. We present evidence that the cycling of PGEs into silicate melt is controlled by physical parameters. The key observation is that molten sulfide behaves physically incompatibly during silicate melt segregation.

Our experiments used as starting composition $(Fe,Ni,Cu)_{1-x}S$ monosulfide synthesized from metal powders and S in evacuated SiO_2 glass tubes at 900°C (*7*). The composition was (in atomic %) 35.6 Fe, 11.8 Ni, 0.7 Cu, and 51.9 S. Ni was calculated assuming that the sulfide is in equilibrium with upper-mantle olivine containing 90 mol % forsterite and 3000 parts per million (ppm) Ni (*8*, *9*). Cu was added assuming that 50% of the Cu in primitive mantle [~20 ppm (*1*)] resides in sulfide. Metal/S was set to 0.93, reflecting a sulfide in moderately oxidized mantle in equilibrium with the fayalite-magnetite-quartz oxygen buffer. The composition was melted between 1040° and 1400°C at 1 atm to 3.5 GPa (*10*).

Phase equilibria at run conditions may be deduced from quench textures (Fig. 1) and from phase compositions (SOM Text). Subsolidus runs resulted in aggregates of ~80-μm-sized polygonal, homogeneous monosulfides that tended to disintegrate after removal from the capsule (Fig. 1A). Experiments with partial sulfide melting, i.e., in the two-phase field, quenched out two phases,

Institut für Mineralogie, Universität Münster, Corrensstrasse 24, 48149 Münster, Germany.

*To whom correspondence should be addressed. E-mail: bockrat@nwz.uni-muenster.de